Pygmy dipole strength in ^{90}Zr

R. Schwengner,[1] G. Rusev,[1,*] N. Tsoneva,[2,3] N. Benouaret,[1,†] R. Beyer,[1] M. Erhard,[1] E. Grosse,[1,4] A. R. Junghans,[1] J. Klug,[1,‡] K. Kosev,[1] H. Lenske,[2] C. Nair,[1] K. D. Schilling,[1] and A. Wagner[1]

[1]*Institut für Strahlenphysik, Forschungszentrum Dresden-Rossendorf, D-01314 Dresden, Germany*

[2]*Institut für Theoretische Physik, Universität Gießen, D-35392 Gießen, Germany*

[3]*Institute for Nuclear Research and Nuclear Energy, BAS, BG-1784 Sofia, Bulgaria*

[4]*Institut für Kern- und Teilchenphysik, Technische Universität Dresden, D-01062 Dresden, Germany*

(Received 18 August 2008; published 19 December 2008)

The dipole response of the $N = 50$ nucleus ^{90}Zr was studied in photon-scattering experiments at the electron linear accelerator ELBE with bremsstrahlung produced at kinetic electron energies of 7.9, 9.0, and 13.2 MeV. We identified 189 levels up to an excitation energy of 12.9 MeV. Statistical methods were applied to estimate intensities of inelastic transitions and to correct the intensities of the ground-state transitions for their branching ratios. In this way we derived the photoabsorption cross section up to the neutron-separation energy. This cross section matches well the photoabsorption cross section obtained from (γ, n) data and thus provides information about the extension of the dipole-strength distribution toward energies below the neutron-separation energy. An enhancement of $E1$ strength has been found in the range of 6 to 11 MeV. Calculations within the framework of the quasiparticle-phonon model ascribe this strength to a vibration of the excessive neutrons against the $N = Z$ neutron-proton core, giving rise to a pygmy dipole resonance.

DOI: 10.1103/PhysRevC.78.064314 PACS number(s): 25.20.Dc, 23.20.Js, 24.30.Gd, 27.60.+j

I. INTRODUCTION

Gamma-ray strength functions, in particular dipole-strength functions, are an important ingredient for the analysis of photodisintegration reactions as well as of the inverse reactions such as neutron capture. These reactions play an important role for specific processes of nucleosynthesis. Moreover, an improved experimental and theoretical description of neutron-capture reactions is important for next-generation nuclear technologies.

The measurement of dipole-strength distributions from low excitation energy up to the neutron-separation energy delivers information about magnitude and structure of the low-energy tail of the giant dipole resonance (GDR), in particular about possible additional vibrational modes such as the so-called pygmy dipole resonance (PDR). Dipole-strength distributions up to neutron-separation energies have been studied for only a few nuclides in experiments with monoenergetic photons (see, e.g., Refs. [1–4]) and in experiments with bremsstrahlung (see, e.g., Ref. [5] and references therein). The bremsstrahlung facility [6] at the superconducting electron accelerator ELBE of the research center Dresden-Rossendorf opens up the possibility to study the dipole response of stable nuclei with even the highest neutron-separation energies in photon-scattering experiments. In the course of a systematic study of dipole-strength distributions for varying neutron and proton numbers in nuclei around $A = 90$ [7,8] we have investigated the $N = 50$ nuclide ^{90}Zr.

In earlier experiments, the 2^+ states at 2186, 3308, 3842, 4120, 4230, and 4680 and the $1^{(-)}$ states at 4580 and 5504 keV were studied with bremsstrahlung produced by 5-MeV electrons [9,10]. About 20 further states were found in experiments at higher energies up to 10 MeV [11,12]. For the 15 $J = 1$ states above 6 MeV negative parity was deduced from an experiment with polarized photons [13].

In the present study we identified about 190 levels up to 12.9 MeV. We applied statistical methods to estimate the intensities of inelastic transitions to low-lying excited levels and to correct the intensities of the elastic transitions to the ground state with their branching ratios. The dipole-strength distribution deduced from the present experiments is compared with predictions of the quasiparticle-phonon model.

II. EXPERIMENTAL METHODS AND RESULTS

The nuclide ^{90}Zr was studied in photon-scattering experiments at the superconducting electron accelerator ELBE of the research center Dresden-Rossendorf. Bremsstrahlung was produced using electron beams of 7.9-, 9.0-, and 13.2-MeV kinetic energy. The average currents were about 330 μA in the measurement at 7.9 MeV and about 500 μA in the measurements at higher energy. The electron beams hit radiators consisting of niobium foils with thicknesses of 4 μm in the low-energy measurements and of 7 μm in the measurement at 13.2 MeV. A 10-cm-thick aluminum absorber was placed behind the radiator to reduce the low-energy part of the bremsstrahlung spectrum (beam hardener). The collimated photon beam impinged onto the target with a flux of about $10^9 s^{-1}$ in a spot of 38 mm in diameter. The target was a disk with a diameter of about 20 mm to enable an irradiation with a

*Present address: Department of Physics, Duke University, and Triangle Universities Nuclear Laboratory, Durham, NC 27708, USA.

†Permanent address: Faculté de physique, Université des Sciences et de la technologie d'Alger, El-Alia 16111, Bab-Ezzouar-Alger, Algerie.

‡Present address: Ringhals Nuclear Power Plant, SE-43022 Väröbacka, Sweden.

constant flux density over the target area. The target consisted of 4054.2 mg of $^{90}ZrO_2$, enriched to 97.7%, combined with 339.5 mg of ^{11}B, enriched to 99.52%, and also formed to a disk of 20 mm in diameter that was used for the determination of the photon flux. Scattered photons were measured with four high-purity germanium (HPGe) detectors of 100% efficiency relative to a NaI detector of 3 in. in diameter and 3 in. in length. All HPGe detectors were surrounded by escape-suppression shields made of bismuth germanate scintillation detectors. Two HPGe detectors were placed vertically at 90° relative to the photon-beam direction at a distance of 28 cm from the target. The other two HPGe detectors were positioned in a horizontal plane at 127° to the beam at a distance of 32 cm from the target. Absorbers of 8 mm Pb plus 3 mm Cu and of 3 mm Pb plus 3 mm Cu were placed in front of the detectors at 90° and 127°, respectively, in the measurements at 7.9 and 9.0 MeV, whereas in the measurement at 13.2 MeV absorbers of 13 mm Pb plus 3 mm Cu and of 8 mm Pb plus 3 mm Cu were used for the detectors at 90° and 127°, respectively. A detailed description of the bremsstrahlung facility is given in Ref. [6].

Spectra of scattered photons were measured for 56 h, 65 h, and 97 h in the experiments at 7.9-, 9.0-, and 13.2-MeV electron energy, respectively. Parts of a spectrum including events measured with the two detectors placed at 127° relative to the beam at an electron energy of 13.2 MeV are shown in Fig. 1.

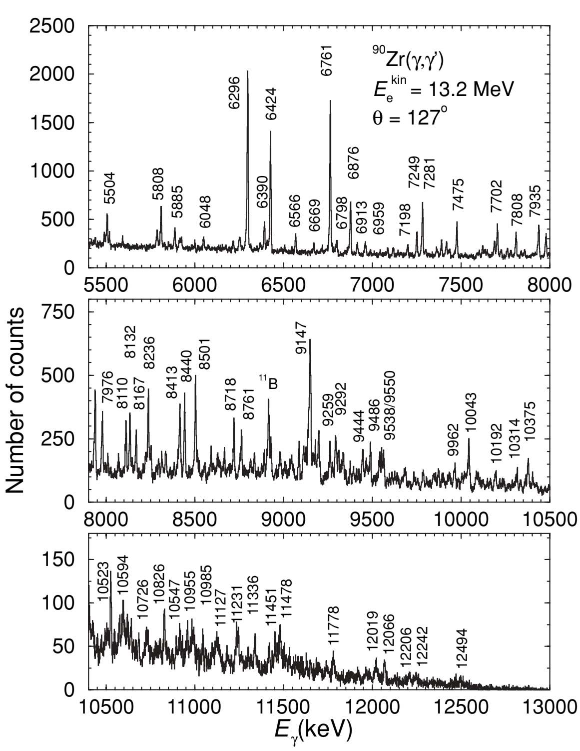

FIG. 1. Parts of a spectrum of photons scattered from ^{90}Zr combined with ^{11}B during the irradiation with bremsstrahlung produced by electrons of an energy of $E_e^{\text{kin}} = 13.2$ MeV. This spectrum is the sum of the spectra measured with the two detectors placed at 127° relative to the beam. The most dominant transitions assigned to ^{90}Zr are marked with their energies in keV.

A. The photon-scattering method

In photon-scattering experiments the energy-integrated scattering cross section I_s of an excited state at the energy E_x can be deduced from the measured intensity of the respective transition to the ground state (elastic scattering). It can be determined relative to the known integrated scattering cross sections $I_s(E_x^{\text{B}})$ of states in ^{11}B [14]:

$$\frac{I_s(E_x)}{I_s(E_x^{\text{B}})} = \left(\frac{I_\gamma(E_\gamma,\theta)}{W(E_\gamma,\theta)\Phi_\gamma(E_x)N_N}\right) \times \left(\frac{I_\gamma(E_\gamma^{\text{B}},\theta)}{W(E_\gamma^{\text{B}},\theta)\Phi_\gamma(E_x^{\text{B}})N_N^{\text{B}}}\right)^{-1}. \quad (1)$$

Here, $I_\gamma(E_\gamma,\theta)$ and $I_\gamma(E_\gamma^{\text{B}},\theta)$ denote the measured intensities of a considered ground-state transition at E_γ and of a ground-state transition in ^{11}B at E_γ^{B}, respectively, observed at an angle θ to the beam. $W(E_\gamma,\theta)$ and $W(E_\gamma^{\text{B}},\theta)$ describe the angular correlations of these transitions. The quantities N_N and N_N^{B} are the numbers of nuclei in the ^{90}Zr and ^{11}B targets, respectively. The quantities $\Phi_\gamma(E_x)$ and $\Phi_\gamma(E_x^{\text{B}})$ stand for the photon fluxes at the energy of the considered level and at the energy of a level in ^{11}B, respectively.

The integrated scattering cross section is related to the partial width of the ground-state transition Γ_0 according to

$$I_s = \int \sigma_{\gamma\gamma}\, dE = \left(\frac{\pi\hbar c}{E_x}\right)^2 \frac{2J_x+1}{2J_0+1}\frac{\Gamma_0^2}{\Gamma}, \quad (2)$$

where $\sigma_{\gamma\gamma}$ is the elastic scattering cross section, E_x, J_x, and Γ denote energy, spin, and total width of the excited level, respectively, and J_0 is the spin of the ground state.

For the determination of the level widths one is faced with two problems. First, a considered level can be fed by transitions from higher lying states. The measured intensity of the ground-state transition is in this case higher than the one resulting from a direct excitation only. As a consequence, the integrated cross section deduced from this intensity contains a part originating from feeding in addition to the true integrated scattering cross section: $I_{s+f} = I_s + I_f$. Furthermore, a considered level can de-excite not only to the ground state but also to low-lying excited states (inelastic scattering). In this case, not all observed γ transitions are ground-state transitions. To deduce the partial width of a ground-state transition Γ_0 and the integrated absorption cross section one has to know the branching ratio $b_0 = \Gamma_0/\Gamma$. If this branching ratio cannot be determined, only the quantity Γ_0^2/Γ can be deduced [cf. Eq. (2)].

Spins of excited states can be deduced by comparing experimental ratios of intensities measured at two angles with theoretical predictions. The optimum combination are angles of 90° and 127° because the respective ratios for the spin sequences 0–1–0 and 0–2–0 differ most at these angles. The expected values are $W(90°)/W(127°)_{0\text{–}1\text{–}0} = 0.74$ and $W(90°)/W(127°)_{0\text{–}2\text{–}0} = 2.18$, taking into account opening angles of 16° and 14° of the detectors at 90° and 127°, respectively.

B. Detector response and photon flux

For the determination of the integrated scattering cross sections according to Eq. (1) the relative efficiencies of the detectors and the relative photon flux are needed. For the determination of the dipole-strength distribution described in Sec. III the experimental spectrum has to be corrected for detector response, for the absolute efficiency, for the absolute photon flux, for background radiation, and for atomic processes induced by the impinging photons in the target material. The detector response has been simulated by using the program package GEANT3 [15]. The reliability of the simulation was tested by comparing simulated spectra with measured ones as described in Refs. [7,8].

The absolute efficiencies of the HPGe detectors were determined experimentally up to 1333 keV from measurements with ^{22}Na, ^{60}Co, ^{133}Ba, and ^{137}Cs calibration sources. The efficiency curve calculated with GEANT3 was scaled to fit the absolute experimental values. To check the simulated efficiency curve at higher energies we used an uncalibrated ^{56}Co source produced in-house using the ^{56}Fe$(p,n)^{56}$Co reaction. The relative efficiency values obtained from the ^{56}Co source adjusted to the calculated value at 1238 keV are consistent with the simulated curve, as is illustrated in Ref. [7].

The absolute photon flux was determined from intensities and known integrated scattering cross sections of transitions in ^{11}B, which was combined with the ^{90}Zr target (cf. Sec. II). For interpolation, the photon flux was calculated by using a code [16] based on the approximation given in Ref. [17] and including a screening correction according to Ref. [18]. In addition, the flux was corrected for the attenuation by the beam hardener. This flux was adjusted to the experimental values as is shown in Fig. 2. The transition from the level at 7285 keV could not be used because of superposition by another transition.

C. Experiments at various electron energies

Measurements at various electron energies allow us to estimate the influence of feeding on the integrated cross

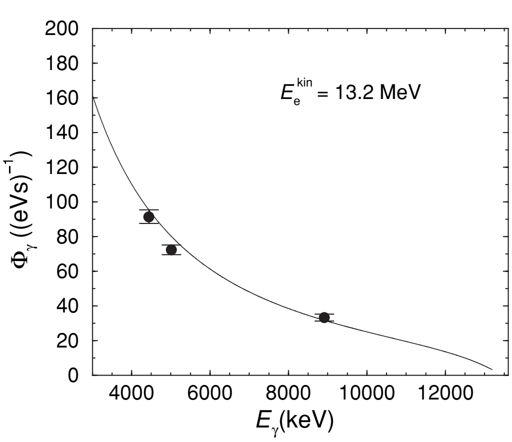

FIG. 2. Absolute photon flux at the target deduced from intensities of transitions in ^{11}B (circles) using the calculated efficiency and the relative photon flux calculated as described in the text (solid line).

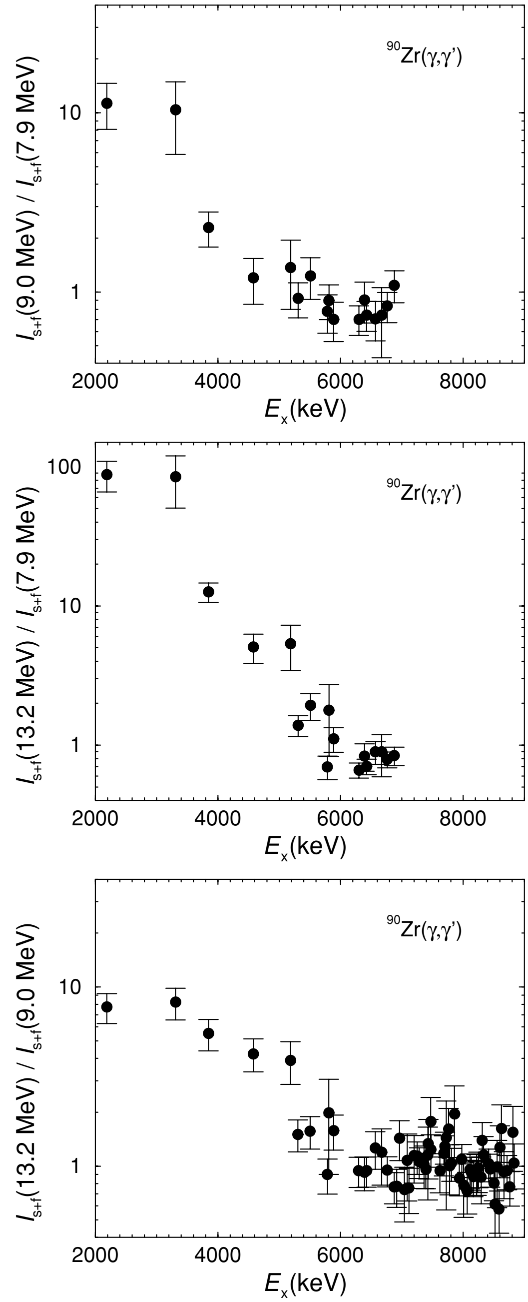

FIG. 3. Ratios of integrated cross sections I_{s+f} of transitions in ^{90}Zr obtained at different electron energies.

sections. Ratios of the quantities I_{s+f} obtained for levels in ^{90}Zr from measurements at different electron energies are shown in Fig. 3.

The plotted ratios reveal that (i) only levels below $E_x \approx$ 6 MeV are influenced considerably by feeding and (ii) levels in the range of $E_x \approx 4$ to 6 MeV are mainly fed by levels above $E_x \approx 9$ MeV. Transitions found in the measurement at $E_e^{\rm kin} = 7.9$ MeV are assumed to be ground-state transitions. Transitions additionally observed up to 7.9 MeV in the measurements at 9.0 and 13.2 MeV are therefore considered as inelastic transitions from high-lying to low-lying excited states. In the same way, transitions in the range from 7 to 9 MeV observed in the measurement at 9.0 MeV are considered as ground-state transitions, whereas transitions in this energy range found additionally at 13.2 MeV are considered as branchings to low-lying states. By comparing the measurements in this way, transitions from high-lying to excited low-lying states may be filtered out. The remaining transitions, assumed as ground-state transitions, have been used to derive the corresponding level energies; these are listed in Table I together with spin assignments deduced from angular distributions of the ground-state transitions, integrated scattering cross sections, and the quantities Γ_0^2/Γ.

In general, the complete level scheme may be constructed by searching for combinations of γ-ray energies that fit another γ-ray according to the Ritz principle. However, if one includes all observed transitions one finds a huge number of possible two-fold or even three-fold combinations [7]. Because we cannot derive complete information about the many possible branching transitions, we are unable to determine the branching ratios of the ground-state transitions from the present data. Therefore, we applied statistical methods to estimate the intensities of branching transitions and thus to correct the dipole-strength distribution.

III. DETERMINATION OF THE DIPOLE-STRENGTH DISTRIBUTION

In the following we describe the statistical methods used to estimate the intensity distribution of branching transitions and the branching ratios of the ground-state transitions.

By using simulations as described in Sec. II B we corrected the spectrum including the two detectors at 127°, measured during the irradiation of the ^{90}Zr target at $E_e^{\mathrm{kin}} = 13.2$ MeV. In a first step, spectra of the ambient background adjusted to the intensities of the 1460.5-keV transition (decay of ^{40}K) and 2614.9-keV transition (decay of ^{208}Tl) in the in-beam spectrum were subtracted from the measured spectrum. It turned out that transitions following (n, γ) reactions in the HPGe detectors and in surrounding materials are negligibly small and thus did not require correction. To correct the spectrum for detector response, spectra of monoenergetic γ rays were calculated in steps of 10 keV by using GEANT3. Starting from the high-energy end of the experimental spectrum, the simulated spectra were subtracted sequentially. The resulting spectrum including the two detectors at 127° is shown in Fig. 4.

The background produced by atomic processes in the ^{90}Zr target was obtained from a GEANT3 simulation by using the absolute photon flux deduced from the intensities of the transitions in ^{11}B (cf. Fig. 2). The corresponding background spectrum multiplied with the efficiency curve and with the measuring time is also depicted in Fig. 4.

As can be seen in Fig. 4 the continuum in the spectrum of photons scattered from ^{90}Zr is clearly higher than the background by atomic scattering. This continuum is formed by a large number of nonresolvable transitions with small intensities; these are a consequence of the increasing nuclear level density at high energy and of Porter-Thomas fluctuations of the decay widths [19] in connection with the finite detector resolution (e.g., $\Delta E \approx 7$ keV at $E_\gamma \approx 9$ MeV).

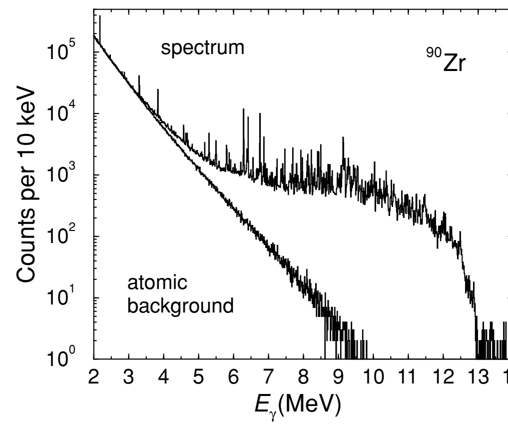

FIG. 4. Experimental spectrum of ^{90}Zr (corrected for room background and detector response) and simulated spectrum of atomic background (multiplied with efficiency and measuring time).

The relevant intensity of the photons resonantly scattered from ^{90}Zr is obtained from a subtraction of the atomic background from the response-corrected experimental spectrum. The remaining intensity distribution includes the intensity contained in the resolved peaks as well as the intensity of the "nuclear" continuum. The scattering cross sections $\sigma_{\gamma\gamma'}$ derived from this intensity distribution for energy bins of 0.2 MeV from the full intensity distribution are shown in Fig. 5. These values are compared with those given in Table I for resolved transitions in ^{90}Zr. One sees that the two curves have similar structures caused by the prominent peaks. However, the curve including also the continuum part of the spectrum contains altogether a strength that is by a factor of about 2.7 greater than the strength of the resolved peaks only.

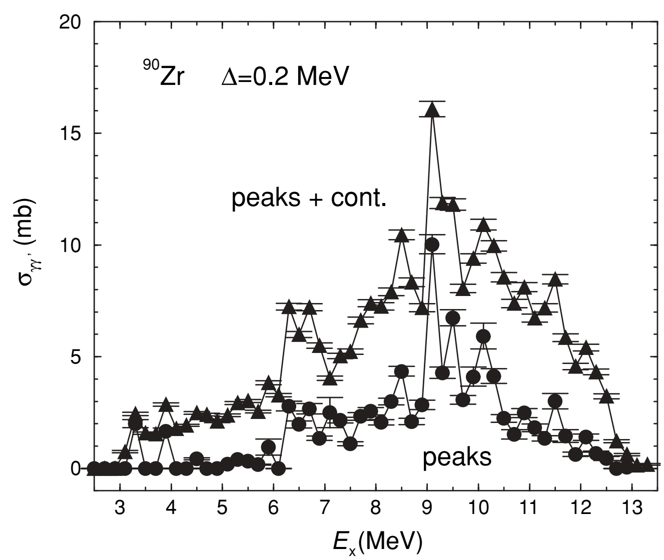

FIG. 5. Scattering cross sections in ^{90}Zr, derived as $\sigma_{\gamma\gamma'} = \sum_\Delta I_s/\Delta$, not corrected for branching and averaged over energy bins of $\Delta = 0.2$ MeV, as derived from the difference of the experimental spectrum and the atomic background shown in Fig. 4 ("peaks + cont.," triangles) and from the resolved peaks only ("peaks," circles).

TABLE I. Levels assigned to ^{90}Zr.

E_x (keV)[a]	$\frac{I_\gamma(90^\circ)}{I_\gamma(127^\circ)}$ [b]	J_x^{π} [c]	$\frac{I_{s+f}(9.0)}{I_{s+f}(7.9)}$ [d]	$\frac{I_{s+f}(13.2)}{I_{s+f}(7.9)}$ [d]	$\frac{I_{s+f}(13.2)}{I_{s+f}(9.0)}$ [d]	I_s (eV b)[e]	Γ_0^2/Γ (meV)[f]
2186.2(1)		2^+[g]	11.3(33)	88(22)	7.7(15)	19(4)	
3308.0(2)		2^+[g]	10.4(45)	85(35)	8.2(17)	4.7(19)	
3842.0(2)		2^+[g]	2.3(5)	12.6(20)	5.5(11)	26(4)	
3932.4(6)						8.3(32)	
4507.0(8)						21(10)	
4578.3(3)			1.2(3)	5.1(12)	4.2(9)	16(4)	
5183.0(5)			1.4(6)	5.4(19)	3.9(10)	7.1(24)	
5304.5(3)			0.92(20)	1.4(2)	1.5(3)	57(8)	
5503.6(3)			1.2(3)	1.9(4)	1.6(3)	34(6)	
5785.0(4)			0.78(19)	0.70(13)	0.90(20)	50(8)	145(22)[h]
5807.9(3)			0.90(20)	1.8(9)	2.0(11)	78(10)	228(30)[h]
5884.4(4)			0.70(17)	1.1(2)	1.6(4)	48(8)	143(23)[h]
6295.8(2)	0.75(3)	1^-[g]	0.70(13)	0.66(8)	0.94(18)	740(63)	2545(218)
6389.8(3)	0.82(8)	1	0.90(23)	0.84(19)	0.93(20)	82(15)	290(54)
6424.3(2)	0.74(4)	1^-[g]	0.74(14)	0.70(9)	0.94(18)	479(43)	1716(153)
6565.7(3)	0.79(15)	1	0.71(18)	0.89(17)	1.3(3)	66(9)	245(34)
6669.2(7)	0.64(16)	1	0.74(31)	0.89(30)	1.2(4)	29(8)	111(32)
6761.4(2)	0.76(3)	1^-[g]	0.83(16)	0.79(10)	0.95(18)	644(60)	2553(237)
6875.4(2)	0.73(4)	1^-	1.09(22)	0.84(13)	0.77(15)	198(22)	813(91)
6960.4(7)	0.77(11)	1			1.4(36)	44(10)	183(41)
7042.0(7)	0.74(19)	1			0.74(25)	25(6)	109(28)
7085.6(10)	0.83(21)	(1)			1.1(4)	30(10)	130(43)
7198.2(6)	0.49(20)	1			1.1(3)	45(10)	201(47)
7249.0(3)	0.78(7)	1^-[g]			1.1(2)	99(17)	450(79)
7280.9(7)[i]							
7361.0(6)	0.57(17)	1			1.0(3)	33(7)	153(33)
7387.6(4)	0.68(10)	1			0.96(21)	75(14)	355(65)
7424.5(10)	1.4(6)				1.1(5)	14(5)	69(24)[h]
7433.8(8)	0.52(21)	1			1.3(5)	19(6)	93(28)
7468(2)	1.5(5)				1.8(6)	12(4)	61(18)[h]
7474.9(3)	0.96(10)	(1)			1.2(3)	127(23)	617(113)
7685.8(4)	0.65(10)	1			1.2(3)	70(13)	358(68)
7702.9(3)	0.83(7)	1^-[g]			1.3(3)	158(28)	815(142)
7723.1(9)	0.9(3)				1.4(9)	20(6)	106(31)[h]
7759.7(6)	0.82(19)	(1)			1.6(5)	38(9)	198(45)
7779.0(6)	0.77(17)	1			1.0(3)	40(9)	212(47)
7807.9(3)	0.75(6)	1			1.0(2)	125(23)	659(120)
7857.8(7)	0.84(25)	(1)			2.0(8)	34(9)	183(50)
7935.6(3)	0.81(6)	1			0.86(17)	209(36)	1141(199)
7976.6(4)	0.67(7)	1			1.1(2)	125(23)	691(124)
8006.9(8)	0.71(25)	1			0.78(27)	36(9)	197(49)
8067.4(5)	0.99(27)	(1)			0.73(19)	55(13)	312(74)
8110.0(8)	0.71(9)	1^-[g]			0.96(21)	124(24)	704(136)
8131.9(4)	0.74(9)	(1^-)[g]			0.93(20)	154(28)	884(164)
8144(2)					20(13)	115(75)[h]	
8166.7(5)	0.89(14)	(1)			0.88(20)	98(19)	566(111)
8221.2(8)	0.80(13)	1			0.92(24)	57(12)	332(73)
8235.6(3)	0.74(4)	1			0.89(18)	254(44)	1495(260)
8250.7(5)	0.68(7)	1			0.98(22)	85(16)	504(98)
8295.3(10)	0.89(29)	(1)			0.87(25)	40(11)	241(67)
8313.0(7)	0.73(18)	1			1.4(4)	70(15)	420(95)
8334.1(5)	0.72(18)	1			1.2(3)	90(20)	539(121)
8357.5(18)	0.32(18)	1				16(7)	97(42)
8382.1(10)	1.1(4)	(1)				25(6)	157(32)
8403.7(11)						43(7)	263(43)[h]
8413.5(4)	0.87(9)	1			1.0(2)	212(38)	1300(235)
8440.6(4)	0.87(10)	1			0.96(20)	224(40)	1382(250)

TABLE I. *(Continued.)*

E_x (keV)[a]	$\frac{I_\gamma(90^\circ)}{I_\gamma(127^\circ)}$ [b]	J_x^π [c]	$\frac{I_{s+f}(9.0)}{I_{s+f}(7.9)}$ [d]	$\frac{I_{s+f}(13.2)}{I_{s+f}(7.9)}$ [d]	$\frac{I_{s+f}(13.2)}{I_{s+f}(9.0)}$ [d]	I_s (eV b)[e]	Γ_0^2/Γ (meV)[f]
8467.7(15)	1.0(5)					31(17)	193(106)
8501.2(4)	0.81(8)	1^-[g]			0.81(17)	346(63)	2166(393)
8518(3)	1.6(6)				0.61(33)	40(16)	253(98)[h]
8544(4)						8(3)	51(19)[h]
8553.5(12)	0.12(6)	1				79(8)	504(50)
8588.3(7)	0.58(13)	1			0.57(15)	93(21)	597(133)
8598.2(10)	0.59(22)	1			1.3(4)	42(12)	270(78)
8625.6(10)	0.72(27)	1			1.6(6)	37(11)	239(69)
8664.1(5)	0.68(16)	1			0.93(27)	59(14)	385(92)
8716.6(5)	0.75(6)	1^-[g]			0.94(20)	176(33)	1162(220)
8751.0(8)	0.36(14)	1				62(15)	410(97)
8760.4(5)	0.58(10)	1			0.77(17)	162(31)	1077(203)
8812.0(13)	0.76(24)	1			1.5(6)	37(13)	246(86)
8833.2(8)	0.67(15)	1			1.0(3)	83(20)	561(134)
8874.9(9)	0.37(13)	1				41(11)	280(75)
8903.0(8)						57(6)	394(43)[h]
8927.4(4)						127(13)	878(91)[h]
8978.4(9)	0.8(4)	(1)				88(31)	615(215)
8985(2)						45(13)	315(90)[h]
9004.7(5)	0.45(23)	1				34(11)	239(78)
9014.0(8)						24(14)	170(101)[h]
9034.0(8)						35(7)	247(50)[h]
9043.6(4)	0.44(6)	1				71(10)	503(68)
9053.5(7)						38(7)	270(49)[h]
9085.1(3)	0.60(9)	1				129(15)	925(109)
9111.1(6)	0.64(15)	1				141(20)	1018(140)
9123.6(7)						126(17)	913(126)[h]
9137.5(7)						185(22)	1338(163)[h]
9148.5(3)	0.60(4)	1^-[g]				703(66)	5103(480)
9164.9(7)						107(14)	778(104)[h]
9177.5(5)						162(18)	1182(134)[h]
9187(3)						45(13)	329(95)[h]
9196.5(3)	0.72(7)	(1^-)[g]				252(25)	1849(186)
9260.5(6)	0.67(9)	1				149(19)	1109(140)
9292.8(5)	0.65(7)	1				216(24)	1619(181)
9309.4(7)	0.71(10)	1				137(18)	1033(135)
9333.4(6)	0.67(10)	1^-[g]				141(19)	1064(146)
9373.2(7)						111(21)	843(161)[h]
9392.4(8)	0.45(13)	1				102(19)	780(145)
9409.4(11)						71(16)	543(123)[h]
9424.3(10)						79(17)	608(129)[h]
9444.7(4)	0.65(8)	1				221(28)	1707(219)
9465.1(5)	0.66(11)	1				169(25)	1317(193)
9486.8(4)	0.75(10)	1				226(32)	1765(251)
9510.5(13)	0.88(35)	(1)				45(16)	350(124)
9524.1(13)	0.47(22)	1				44(14)	348(112)
9539.2(5)	0.85(13)	1				154(22)	1213(175)
9551.4(6)	0.47(9)	1				160(23)	1267(185)
9563.0(6)	0.64(17)	1				180(28)	1424(221)
9609.2(7)						72(22)	573(177)[h]
9625.1(8)						58(16)	469(129)[h]
9640.4(8)	0.6(3)	1				56(14)	456(115)
9666.0(8)	0.7(3)	(1)				39(9)	318(71)
9678.3(7)	0.67(19)	(1^-)[g]				67(10)	545(83)
9686.9(6)	0.66(17)	1				72(11)	591(89)
9733.2(5)	0.5(3)	1				55(8)	450(68)
9741.7(7)						33(6)	275(51)[h]

TABLE I. *(Continued.)*

E_x (keV)[a]	$\frac{I_\gamma(90^\circ)}{I_\gamma(127^\circ)}$ [b]	J_x^π [c]	$\frac{I_{s+f}(9.0)}{I_{s+f}(7.9)}$ [d]	$\frac{I_{s+f}(13.2)}{I_{s+f}(7.9)}$ [d]	$\frac{I_{s+f}(13.2)}{I_{s+f}(9.0)}$ [d]	I_s (eV b)[e]	Γ_0^2/Γ (meV)[f]
9754.0(6)	0.46(29)	1				50(9)	413(71)
9784.6(5)	1.37(27)					111(15)	921(122)[h]
9805.4(10)	1.6(6)					41(9)	341(73)[h]
9843.4(6)	0.77(16)	1				84(15)	702(126)
9855.5(8)	0.55(17)	1				58(13)	488(109)
9872.4(4)	0.49(12)	1				126(24)	1067(207)
9890.7(13)	0.7(5)	(1)				81(34)	686(289)
9901.9(13)						70(28)	592(242)[h]
9932.1(12)	0.43(14)	1				123(39)	1053(330)
9962.8(5)	0.57(14)	1				172(37)	1479(322)
9984.1(11)						69(34)	593(297)[h]
10004.2(10)	0.42(19)	1				70(16)	606(137)
10019.6(11)	0.65(16)	1				94(16)	819(138)
10031(2)						69(16)	599(136)[h]
10042.9(4)	0.70(8)	(1^-)[g]				316(36)	2762(310)
10083.8(6)	0.78(13)	1				93(13)	823(118)
10094.2(7)	0.74(19)	1				83(14)	732(120)
10104.9(12)	0.7(3)	(1)				49(13)	433(118)
10123.7(18)	0.5(3)	1				137(100)	1219(886)
10146.8(9)	0.57(27)	1				46(13)	409(114)
10163.4(8)	0.50(23)	1				60(16)	540(147)
10193.0(5)	0.60(12)	1				168(25)	1514(220)
10216.8(10)	0.57(24)	1				76(18)	693(159)
10233(4)						47(38)	427(348)[h]
10241(2)	0.9(3)	(1)				79(34)	723(305)
10260.9(11)						23(6)	212(53)[h]
10270.0(7)						34(9)	308(81)[h]
10286.2(6)	0.64(19)	1				42(9)	388(79)
10298.3(10)	0.8(3)	(1)				32(8)	290(69)
10306.6(9)	0.71(21)	1				46(9)	426(80)
10315.1(4)	0.63(12)	1				103(14)	952(126)
10334.9(6)	0.68(21)	1				51(10)	470(93)
10361(2)	0.86(29)	(1)				54(14)	504(129)
10376.8(4)	0.46(7)	1				240(28)	2240(259)
10402.5(9)	0.72(14)	1				85(16)	799(150)
10494.5(11)	0.7(3)	(1)				43(10)	411(92)
10507.9(8)	0.6(3)	1				49(10)	467(96)
10524.6(4)	0.72(10)	1				143(18)	1376(175)
10595.0(7)	0.80(19)	1				92(14)	901(136)
10618.7(8)	0.74(23)	1				67(12)	651(119)
10638.5(9)	0.41(20)	1				59(12)	575(122)
10682.2(6)	0.54(16)	1				42(10)	417(95)
10713.2(12)	0.8(4)	(1)				37(20)	369(195)
10728.2(11)	0.67(20)	1				102(32)	1022(316)
10827.1(5)	0.82(15)	1				105(16)	1068(167)
10914(2)	0.79(21)	(1)				113(21)	1168(214)
10957(2)	0.35(8)	1				118(19)	1224(202)
10987.0(10)	0.66(13)	1				161(23)	1691(242)
11044(2)						49(17)	522(179)[h]
11094.2(15)						70(10)	743(106)[h]
11108.0(16)						39(8)	422(84)[h]
11120.4(9)	0.60(16)	1				92(17)	992(179)
11129.2(17)						57(18)	611(196)[h]
11140(2)						57(9)	612(95)[h]
11232.4(7)	0.45(14)	1				88(13)	963(146)
11243.2(6)	0.58(15)	1				92(14)	1010(152)
11337.7(6)	0.85(13)	1				91(15)	1010(167)

TABLE I. *(Continued.)*

E_x (keV)[a]	$\frac{I_\gamma(90^\circ)}{I_\gamma(127^\circ)}$ [b]	J_x^π [c]	$\frac{I_{s+f}(9.0)}{I_{s+f}(7.9)}$ [d]	$\frac{I_{s+f}(13.2)}{I_{s+f}(7.9)}$ [d]	$\frac{I_{s+f}(13.2)}{I_{s+f}(9.0)}$ [d]	I_s (eV b)[e]	Γ_0^2/Γ (meV)[f]
11417.5(7)	0.8(4)	(1)				108(25)	1217(287)
11452.2(10)	0.42(12)	1				132(28)	1501(316)
11479.7(8)	0.58(15)	1				191(33)	2181(374)
11501(3)						66(37)	756(425)[h]
11510(7)						33(15)	382(172)[h]
11531(2)	0.42(25)	1				74(30)	848(346)
11627.9(9)						44(16)	518(182)[h]
11651.5(8)	1.0(3)	(1)				48(16)	564(185)
11777.4(10)	0.46(22)	1				124(40)	1489(479)
11788(3)	0.44(29)	1				73(36)	885(440)
11963.3(18)	0.8(3)	(1)				68(14)	845(179)
11984(2)	0.57(18)	1				57(13)	715(167)
12020.6(8)	0.67(14)	1				155(21)	1942(260)
12067.8(9)	0.63(17)	1				124(19)	1570(237)
12208.3(12)	0.40(15)	1				72(16)	929(214)
12243.6(14)	0.57(19)	1				62(15)	799(188)
12496.3(18)						87(18)	1181(244)[h]
12880.3(10)						11(3)	164(46)[h]

[a]Excitation energy. The uncertainty in parentheses is given in units of the last digit. This energy was deduced from the γ-ray energy measured at 127° to the beam byincluding a recoil and Doppler correction.
[b]Ratio of the intensities of the ground-state transitions measured at angles of 90° and 127°. The expected values for an elastic pure-dipole transition (spin sequence 0–1–0) and for an elastic quadrupole transition (spin sequence 0–2–0) are 0.74 and 2.18, respectively.
[c]Spin and parity of the state.
[d]Ratio of integrated scattering plus feeding cross sections deduced at different electron energies. The deviation from unity is a measure of feeding.
[e]Integrated scattering cross section. The values up to the level at 6875 keV were deduced from the measurement at $E_e^{\mathrm{kin}} = 7.9$ MeV, those from the level at 6960 keV up to the level at 8832 keV were deduced from the measurement at $E_e^{\mathrm{kin}} = 9.0$ MeV, and the values given for levels at higher energies were deduced from the measurement at $E_e^{\mathrm{kin}} = 13.2$ MeV.
[f]Partial width of the ground-state transition Γ_0 multiplied with the branching ratio $b_0 = \Gamma_0/\Gamma$. The values deduced from the given I_s for states up to the 5504-keV state exceed the values of previous studies [12] outside their uncertainties, which may indicate that the present values are influenced by feeding. These values are therefore not given in this table. An estimate of the partial width Γ_0 can be obtained from Γ_0^2/Γ after correction for a mean branching ratio $b_0 = \Gamma_0/\Gamma = 0.9(1)\%$ for resolved ground-state transitions (cf. Sec. III).
[g]Spin and parity have been known from previous work (cf. Sec. I).
[h]Value deduced under the assumption of $J_x = 1$.
[i]This transition is superimposed by a transition in ^{11}B.

The full intensity distribution (resolved peaks and continuum) and the corresponding scattering cross sections shown in Fig. 5 contain ground-state transitions and, in addition, branching transitions to lower lying excited states (inelastic transitions) as well as transitions from those states to the ground state (cascade transitions). The different types of transitions cannot be clearly distinguished. However, for the determination of the photoabsorption cross section and the partial widths Γ_0 the intensities of the ground-state transitions are needed. Therefore, contributions of inelastic and cascade transitions have to be subtracted from the spectra. We corrected the intensity distributions by simulating γ-ray cascades [20] from the levels with $J = 0, 1, 2$ in the whole energy range analogously to the strategy of the Monte Carlo code DICEBOX [21]. In these simulations, 1000 nuclear realizations starting from the ground state were created with level densities derived from experiments [22]. We applied the statistical methods also for the low-energy part of the level scheme instead of using experimentally known low-lying levels in ^{90}Zr because this would require the knowledge of the partial decay widths of all transitions populating these fixed levels. Fluctuations of the nearest-neighbor spacings were taken into account according to the Wigner distribution (see, e.g., Ref. [23]). The partial widths of the transitions to low-lying levels were assigned using *a priori* known strength functions for $E1$, $M1$, and $E2$ transitions. Fluctuations of the partial widths were treated the applying Porter-Thomas distribution [19].

In the calculations, the recently published parameters for the back-shifted Fermi-gas (BSFG) model obtained from fits to experimental level densities [22], $a = 8.95(41)$ MeV^{-1} and $E_1 = 1.97(30)$ MeV, were used. In the individual nuclear realizations, the values of a and E_1 were varied within their uncertainties. As usual in the BSFG model, we assumed equal level densities for states with positive and negative parities of the same spin [22]. This assumption has recently been justified by the good agreement of level densities predicted by the BSFG model with experimental level densities of 1^+ states in the energy range from 5 to 10 MeV obtained from the ^{90}Zr(^{3}He, t)^{90}Nb reaction [24] and with experimental level densities of 2^+ and 2^- states in ^{90}Zr studied in the ^{90}Zr(e, e') and ^{90}Zr(p, p') reactions [25]. The extended analysis of the ^{90}Zr(^{3}He, t)^{90}Nb reaction in Ref. [25] indicates however fluctuations of the level density of 1^+ states in ^{90}Nb around the predictions of the BSFG model.

For the $E1$, $M1$, and $E2$ photon strength functions Lorentz parametrizations [26] were used. The parameters of the Lorentz curve for the $E1$ strength were taken from a fit to (γ, n) data [27] and are consistent with the Thomas-Reiche-Kuhn (TRK) sum rule $\frac{\pi}{2}\sigma_0\Gamma = 60NZ/A$ MeV mb [28]. The parameters for the $M1$ and $E2$ strengths were taken from global parametrizations of $M1$ spin-flip resonances and $E2$ isoscalar resonances, respectively [29].

Spectra of γ-ray cascades were generated for groups of levels in 100-keV bins in each of the 1000 nuclear realizations. For illustration, the distributions resulting from 10 individual nuclear realizations populating levels in a 100-keV bin around 9 MeV are shown in Fig. 6, which reflect the influence of fluctuations of level energies and level widths. Because in the nuclear realizations the levels were created randomly starting from the ground state instead of starting with the known first excited state at 2.2 MeV, the distribution of the branching transitions continues to the energy bin of the ground-state transitions.

These spectra resemble qualitatively the ones measured in an experiment on ^{90}Zr using tagged photons [4]. Starting from the high-energy end of the experimental spectrum, which contains ground-state transitions only, the simulated intensities of the ground-state transitions were normalized to the experimental ones in the considered bin and the intensity distribution of the branching transitions was subtracted from the experimental spectrum. Applying this procedure step by step for each energy bin moving toward the low-energy end of the spectrum one obtains the intensity distribution of the ground-state transitions. Simultaneously, the branching ratios b_0^Δ of the ground-state transitions are deduced for each energy bin Δ. In an individual nuclear realization, the branching ratio b_0^Δ is calculated as the ratio of the sum of the intensities of the ground-state transitions from all levels in Δ to the total intensity of all transitions depopulating those levels to any low-lying levels including the ground state [7,8]. By dividing the summed intensities in a bin of the experimental intensity distribution of the ground-state transitions by the corresponding branching ratio we obtain the absorption cross section for a bin as $\sigma_\gamma^\Delta = \sigma_{\gamma\gamma}^\Delta / b_0^\Delta$. Finally, the absorption cross sections of each bin were obtained by averaging over the values of the 1000 nuclear realizations. For the uncertainty of the absorption cross section a 1σ deviation from the mean has been taken.

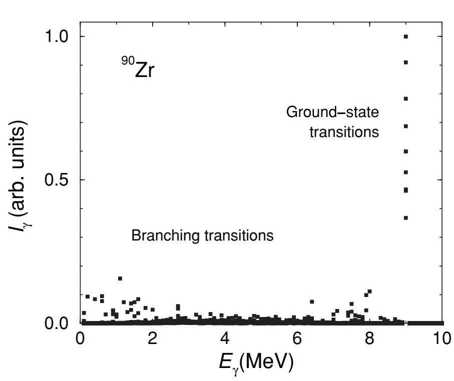

FIG. 6. Simulated intensity distribution of transitions depopulating levels in a 100-keV bin around 9 MeV in ^{90}Zr. The squares depict the intensities obtained from 10 individual nuclear realizations.

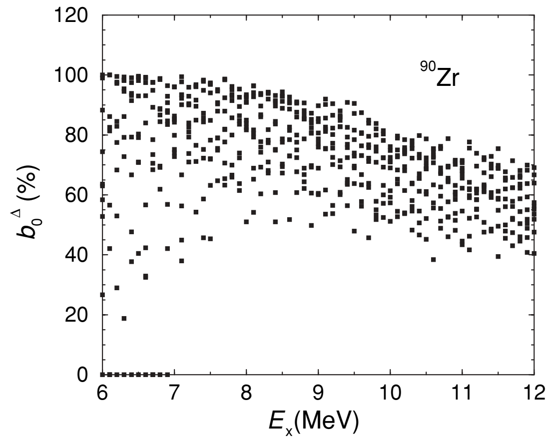

FIG. 7. Branching ratios of ground-state transitions as obtained from the simulations of γ-ray cascades for ^{90}Zr. The squares represent the values of 10 individual nuclear realizations.

To get an impression about the branching ratios, the individual values of 10 nuclear realizations are shown in Fig. 7. The mean branching ratio of the 1000 realizations decreases from about 80% for low-lying states, where only few possibilities for transitions to lower lying states exist, to about 65% at the neutron-separation energy. Toward low energy the uncertainty of b_0^Δ increases because of level-spacing fluctuations and the decreasing level density. The large fluctuations below about 6 MeV make these values useless. Note that the mean branching ratio is not representative for transitions with large intensities such as the resolved transitions given in Table I. It turns out from the simulations that the branching ratios of transitions with partial widths Γ_0 like the ones given in Table I are in the order of $b_0 \approx 85\%$ to 99% (cf. also Ref. [7]).

The photoabsorption cross sections obtained for ^{90}Zr are compared with the data of a previous experiment with monoenergetic photons in the energy range from 8.4 to 12.5 MeV [1] in Fig. 8. The data of Ref. [1] contain corrections in the form of additional constant partial widths for branching and for proton emission [i.e., for the (γ, p) channel]. Cross sections obtained in (γ, n) experiments [27] and cross sections calculated for the (γ, p) reaction by using the TALYS code [30] with the Lorentz model for the $E1$ strength function [26] are also shown in Fig. 8.

To test the influence of the $E1$ strength function on the results of the simulation and to check the consistency between input strength function and deduced photoabsorption cross section we performed cascade simulations with modified $E1$ strength functions. In one case, we applied a Lorentz curve

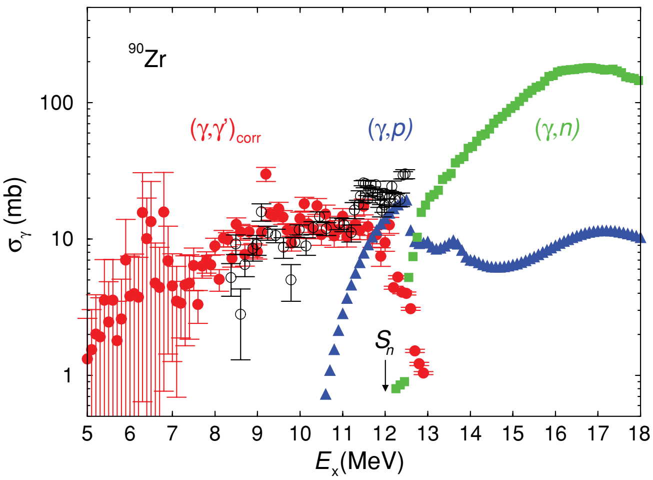

FIG. 8. (Color online) Photoabsorption cross section deduced from the present (γ,γ') data for ^{90}Zr after correction for branching transitions (red circles) in comparison with data obtained from an experiment with monoenergetic photons (open black circles) [2], (γ,n) data taken from Ref. [27] (green boxes), and (γ,p) cross sections calculated with the TALYS code [30] (blue triangles).

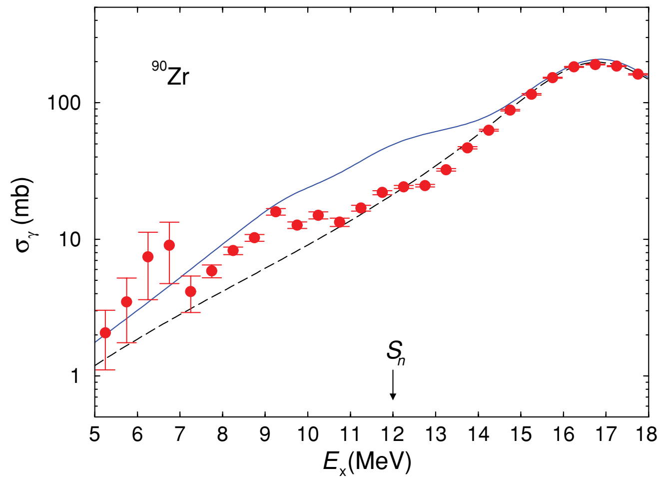

FIG. 10. (Color online) Total photoabsorption cross section of ^{90}Zr obtained by combining the present (γ,γ') data, the (γ,n) data of Ref. [27], and the (γ,p) calculations of Ref. [30]. The data were averaged over 0.5-MeV bins to reduce statistical fluctuations. The black dashed line represents a Lorentz curve with the parameters taken from Ref. [27], as also shown in Fig. 9. The blue solid line is the result of QRPA calculations discussed in Sec. IV B.

with an energy-dependent width $\Gamma(E) \sim E$. In another case we assumed a PDR on top of the Lorentz curve with constant width. The PDR had a Breit-Wigner shape with its maximum at 9 MeV and a width of 2 MeV. The cross section of the PDR was chosen as 2.2% of the TRK (see discussion in Sec. IV B). Cross sections corresponding to these input strength functions and the obtained absorption cross sections are shown in Fig. 9. One sees that the resulting absorption cross sections differ only slightly from each other and also from the ones obtained by using the Lorentz curve with constant width (cf. Fig. 8) and overlap within their uncertainties. This shows that the resulting cross sections are not very sensitive to modifications of the input strength functions. However, the comparison of the resulting cross sections with the input strength functions shows that there is consistency in the case of the Lorentz curve with a PDR in addition, whereas there is a large discrepancy in the case of the Lorentz curve with energy-dependent width. In summary, the Lorentz curve with a constant width and this curve with a PDR in addition deliver consistency between input and output strength functions and similar results.

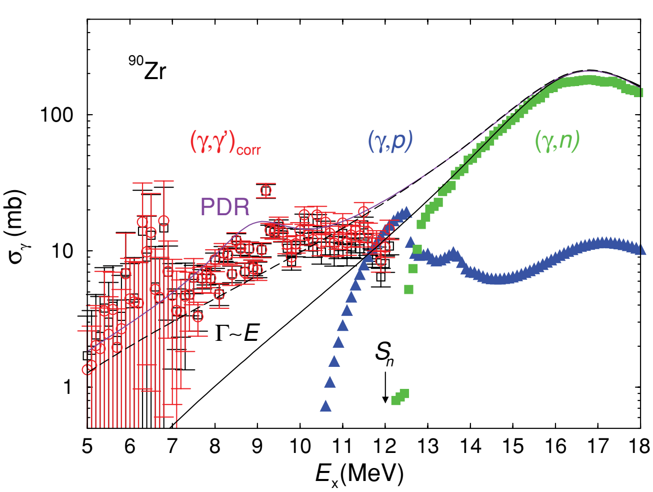

FIG. 9. (Color online) Photoabsorption cross sections deduced from the present (γ,γ') data for ^{90}Zr like the red circles in Fig. 8, but with modified $E1$ strength functions. The black squares are the results for a Lorentz curve with energy-dependent width (black line) and the red circles are the results for the assumption of a PDR on top of a Lorentz curve with constant width (pink line). The Lorentz curve with a constant width and without PDR is shown as a black dashed line.

The total photoabsorption cross section has been deduced by combining the present (γ,γ') data with the (γ,n) data of Ref. [27] and calculated (γ,p) cross sections [30]. This total cross section is compared with the Lorentz curve just described, which is currently used as a standard strength function for the calculation of reaction data [29], in Fig. 10. It can be seen that the experimental cross section includes extra strength with respect to the approximation of the low-energy tail of the GDR by a Lorentz curve in the energy range from 6 to 11 MeV and is in better agreement with a strength function including a PDR on top of the Lorentz curve (cf. Fig. 9). To investigate the nature of this extra strength we have performed model calculations. These are discussed in the following section.

IV. QUASIPARTICLE-PHONON-MODEL CALCULATIONS FOR THE $N = 50$ ISOTONES ^{88}Sr AND ^{90}Zr

The experimental data on the dipole response of ^{90}Zr discussed in the present work reveal a strong enhancement of the photoabsorption cross section (see Fig. 10) in the energy range $E_x = 6$–11 MeV and a considerable deviation of its shape from the Lorentz-like strength function used to adjust the GDR. Similar dipole resonance structures have been detected also in our recent study of ^{88}Sr [7]. In the following we investigate the nature of the dipole strength in the $N = 50$ isotones ^{88}Sr and ^{90}Zr in the framework of the extended quasiparticle-phonon model (QPM) [31,32]. The approach is based on a Hartree-Fock-Bogoljubov (HFB) description of the ground state [31] by using a phenomenological energy-density functional (EDF) [32]. The excited states are calculated within the QPM [33].

A. The QPM model

The model Hamiltonian is given by

$$H = H_{\rm MF} + H_M^{\rm ph} + H_{\rm SM}^{\rm ph} + H_M^{\rm pp} \tag{3}$$

and resembles in structure that of the traditional QPM model [33] but in detail differs in the physical content in important aspects as discussed in Refs. [31,32]. The HFB term $H_{\rm MF} = H_{\rm sp} + H_{\rm pair}$ contains two parts. $H_{\rm sp}$ describes the motion of protons and neutrons in a static, spherically symmetric mean field, and $H_{\rm pair}$ accounts for the monopole pairing between isospin-identical particles with phenomenologically adjusted coupling constants, fitted to data [34]. The mean-field Hamiltonian compromises microscopic HFB effects [32,35] and phenomenological aspects such as experimental separation energies and, when available, also charge and mass radii. For numerical convenience the mean-field potential is parametrized in terms of a superpositions of Wood-Saxon (WS) potentials with adjustable parameters [32].

The remaining three terms present the residual interaction $H_{\rm res} = H_M^{\rm ph} + H_{\rm SM}^{\rm ph} + H_M^{\rm pp}$. As typical for the QPM, we use separable multipole-multipole $H_M^{\rm ph}$ and spin-multipole $H_{\rm SM}^{\rm ph}$ interactions both of isoscalar and isovector type in the particle-hole channel and a multipole-multipole pairing $H_M^{\rm pp}$ in the particle-particle channel. The isoscalar and isovector coupling constants are obtained by a fit to energies and transition strengths of low-lying vibrational states and high-lying GDRs [32,36].

The excited nuclear states are described by quasiparticle-random-phase-approximation (QRPA) phonons. They are defined as a linear combination of two-quasiparticle creation and annihilation operators:

$$Q^+_{\lambda\mu i} = \frac{1}{2}\sum_{jj'}\left(\psi^{\lambda i}_{jj'}A^+_{\lambda\mu}(jj') - \varphi^{\lambda i}_{jj'}\widetilde{A}_{\lambda\mu}(jj')\right), \tag{4}$$

where $j \equiv (nljm\tau)$ is a single-particle proton or neutron state, and $A^+_{\lambda\mu}$ and $\widetilde{A}_{\lambda\mu}$ are time-forward and time-backward operators, coupling proton and neutron two-quasiparticle creation or annihilation operators to a total angular momentum λ with projection μ by means of the Clebsch-Gordan coefficients $C^{\lambda\mu}_{jmj'm'} = \langle jmj'm'|\lambda\mu\rangle$. The time reversed operator is defined as $\widetilde{A}_{\lambda\mu} = (-)^{\lambda-\mu}A_{\lambda-\mu}$.

We take into account the intrinsic fermionic structure of the phonons by the commutation relations

$$\begin{aligned}
&[Q_{\lambda\mu i}, Q^+_{\lambda'\mu' i'}]\\
&\quad = \frac{\delta_{\lambda,\lambda'}\delta_{\mu,\mu'}\delta_{i,i'}}{2}\sum_{jj'}\left[\psi^{\lambda i}_{jj'}\psi^{\lambda i'}_{jj'} - \varphi^{\lambda i}_{jj'}\varphi^{\lambda i'}_{jj'}\right]\\
&\qquad - \sum_{\substack{jj'j_2\\ mm'm_2}}\alpha^+_{jm}\alpha_{j'm'} \times \left\{\psi^{\lambda i}_{j'j_2}\psi^{\lambda' i'}_{jj_2}C^{\lambda\mu}_{j'm'j_2m_2}C^{\lambda'\mu'}_{jmj_2m_2}\right.\\
&\qquad \left. - (-)^{\lambda+\lambda'+\mu+\mu'}\varphi^{\lambda i}_{jj_2}\varphi^{\lambda' i'}_{j'j_2}C^{\lambda-\mu}_{jmj_2m_2}C^{\lambda'-\mu'}_{j'm'j_2m_2}\right\}.
\end{aligned} \tag{5}$$

The QRPA phonons obey the equation of motion

$$[H, Q^+_i] = E_i Q^+_i, \tag{6}$$

which solves the eigenvalue problem (i.e., it gives the excitation energies E_i and the time-forward and time-backward amplitudes [33] $\psi^{\lambda i}_{j_1j_2}$ and $\varphi^{\lambda i}_{j_1j_2}$, respectively).

In terms of the QRPA phonons the model Hamiltonian can be expressed as

$$\begin{aligned}
H = H_{\rm ph} + H_{\rm qph} &= \sum_{\lambda\mu i}\omega_{\lambda i}Q^+_{\lambda\mu i}Q_{\lambda\mu i}\\
&\quad + \frac{1}{2}\sum_{\lambda_1\lambda_2\lambda_3 i_1 i_2 i_3\mu_1\mu_2\mu_3} C^{\lambda_3-\mu_3}_{\lambda_1\mu_1\lambda_2\mu_2}U^{\lambda_2 i_2}_{\lambda_1 i_1}(\lambda_3 i_3)\\
&\quad \times \left[Q^+_{\lambda_1\mu_1 i_1}Q^+_{\lambda_2\mu_2 i_2}Q_{\lambda_3-\mu_3 i_3} + \text{h.c.}\right].
\end{aligned} \tag{7}$$

The first part in the Eq. (7) refers to the harmonic part of nuclear vibrations; the second accounts for the interaction between quasiparticles and phonons. The latter allows us to go beyond the ideal harmonic picture by including effects resulting from the nonbosonic features of the nuclear excitations.

The model Hamiltonian is diagonalized by assuming a spherical 0^+ ground state, which leads to an orthonormal set of wave functions with good total angular momentum JM. For even-even nuclei we extend the approach to anharmonic effects by considering wave functions including a mixture of one-, two-, and three-phonon components [37]:

$$\begin{aligned}
&\Psi_\nu(JM)\\
&= \left\{\sum_i R_i(J\nu)Q^+_{JMi} + \sum_{\substack{\lambda_1 i_1\\ \lambda_2 i_2}}P^{\lambda_1 i_1}_{\lambda_2 i_2}(J\nu)\left[Q^+_{\lambda_1\mu_1 i_1}\times Q^+_{\lambda_2\mu_2 i_2}\right]_{JM}\right.\\
&\quad \left. + \sum_{\substack{\lambda_1 i_1\lambda_2 i_2\\ \lambda_3 i_3 I}}T^{\lambda_1 i_1\lambda_2 i_2 I}_{\lambda_3 i_3}(J\nu)\left[\left[Q^+_{\lambda_1\mu_1 i_1}\otimes Q^+_{\lambda_2\mu_2 i_2}\right]_{IK}\otimes Q^+_{\lambda_3\mu_3 i_3}\right]\right\}_{JM}\\
&\quad \times \Psi_0,
\end{aligned} \tag{8}$$

where ν labels the number of the excited states. The energies and the phonon-mixing amplitudes R, P, and T are determined by solving the extended multiphonon equations of motions.

As discussed in Refs. [32,38] we obtain important additional information from the analysis of the spatial structure of the nuclear response on an external electromagnetic field. That information is accessible by considering the one-body transition densities $\delta\rho(\vec{r})$, which are the nondiagonal elements of the nuclear one-body density matrix. The transition densities

TABLE II. HFB results obtained with the phenomenological EDF for total binding energy per nucleon, the measured binding energy [34], proton and neutron root-mean-square radii, and neutron skin thickness, Eq. (9), for the two $N = 50$ isotones.

	$\frac{B(A)}{A}_{\text{exp}}$ (MeV)	$\frac{B(A)}{A}_{\text{the}}$ (MeV)	$\sqrt{r_p^2}$ (fm)	$\sqrt{r_n^2}$ (fm)	δr (fm)
^{88}Sr	–8.733	–8.766	4.185	4.291	0.106
^{90}Zr	–8.710	–8.692	4.229	4.303	0.074

are obtained by the matrix elements between the ground state $|\Psi_i\rangle = |J_i M_i\rangle$ and the excited states $|\Psi_f\rangle = |J_f M_f\rangle$. We identify in QPM $|J_i M_i\rangle \equiv |0\rangle$ with phonon vacuum and obtain the excited states by means of the QRPA state operator, Eq. (4), $|J_f M_f\rangle \equiv Q^+_{\lambda\mu i}|0\rangle$. The analytical procedure for the calculation of the transition densities is presented in detail in Ref. [32].

B. Calculation of dipole excitations in the $N = 50$ isotones

In Ref. [32], a close relationship between skins in the ground-state matter-density distributions and the low-energy dipole response was pointed out. It was shown that the skin thickness, defined by

$$\delta r = \sqrt{\langle r_n^2\rangle} - \sqrt{\langle r_p^2\rangle}, \tag{9}$$

is indeed directly connected to the non-energy-weighted dipole sum rule, thus being complementary to the well-established relation of the GDR strength and the energy-weighted TRK dipole sum rule. From the calculated neutron and proton ground-state densities displayed in Fig. 11 it is seen that the two $N = 50$ isotones considered here, ^{88}Sr and ^{90}Zr, show a neutron skin. The total binding energies and radii are given in Table II. Of special importance for our investigations are the surface regions, where the formation of a skin takes place. For the investigated ^{88}Sr and ^{90}Zr nuclei, the neutron skin decreases with decreasing N/Z (i.e., when going from ^{88}Sr to ^{90}Zr).

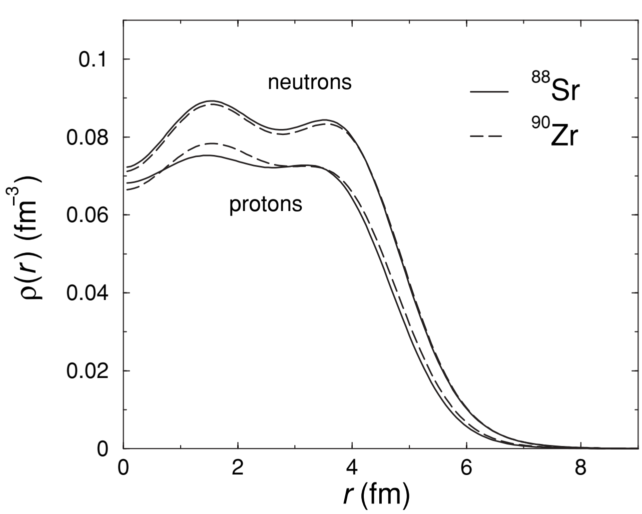

FIG. 11. Proton and neutron ground-state densities of the $N = 50$ isotones ^{88}Sr and ^{90}Zr.

The QRPA calculations in these nuclei result in a sequence of low-lying one-phonon dipole states of almost pure neutron structure, located below the particle threshold. The proton contribution in the state vectors is less than 5%. These states have been related to the oscillations of weakly bound neutrons from the surface region, known as neutron PDR (see Refs. [31,32,38–40] and references therein). The calculations of the dipole response in $N = 50$ up to 22 MeV are presented in Fig. 12. The $E1$ transition matrix elements were calculated with recoil-corrected effective charges $q_n = -Z/A$ for neutrons and $q_p = N/A$ for protons [32], respectively. To compare the predicted dipole strengths with the experimental values we calculated the integrated absorption cross sections according to $\int \sigma_\gamma \, dE = 4.03 E_x B(E1, 0^+ \rightarrow 1^-)$ MeV mb with E_x in MeV and $B(E1)$ in e^2 fm^2 [41]. When comparing the QRPA results with experimental cross sections one has the general problem of comparing discrete values (cf. Fig. 12) with gradually changing averages of energy bins (cf. Fig. 10). Therefore, the QRPA values are usually folded with Lorentz curves that can be considered as a simulation of the damping of the GDR by higher order configurations neglected in QRPA. In the present case, we folded the discrete QRPA cross sections with Lorentz curves of 3.0 MeV width, which is a typical value for the damping width. The results are compared with the experimental cross sections in Fig. 10 for ^{90}Zr and in

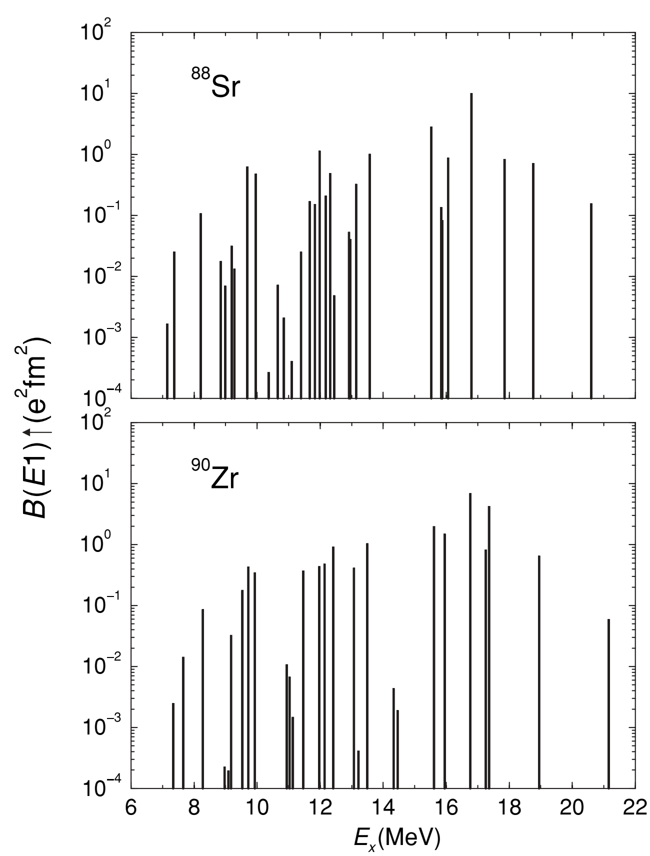

FIG. 12. Calculated dipole one-phonon transition strengths up to $E_x = 22$ MeV for the isotones ^{88}Sr and ^{90}Zr.

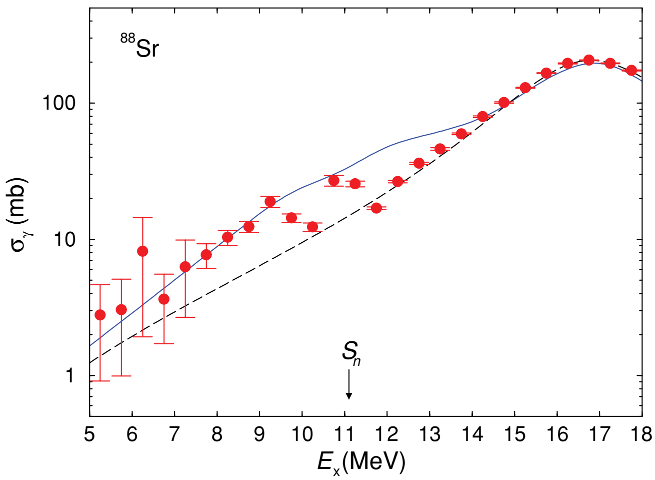

FIG. 13. (Color online) Total photoabsorption cross section of ^{88}Sr as taken from Ref. [7]. The black dashed line represents a Lorentz distribution with the parameters given in Ref. [7]. The blue solid line is the result of the present QRPA calculations.

Fig. 13 for ^{88}Sr. The QRPA calculations predict extra strength with respect to the Lorentz curve, in qualitative agreement with the experimental findings. However, the experimental cross sections show a clear separation of the PDR and the GDR regions around 12 MeV, whereas the calculations seem to predict an excess of strength up to about 14 MeV.

The nature of the dipole strength can be examined by analyzing dipole transition densities that act as a clear indicator of the PDR and allow us to distinguish among the different types of the dipole excitations [32]. The QRPA proton and neutron dipole transition densities for ^{88}Sr and ^{90}Zr were summed over selected energy regions and are shown in Fig. 14. They can be directly related to the spectrum of 1^- states in Fig. 12. In the region of $E_x < 9$ MeV we find an in-phase oscillation of protons and neutrons in the nuclear interior, whereas at the surface only neutrons contribute. Because these

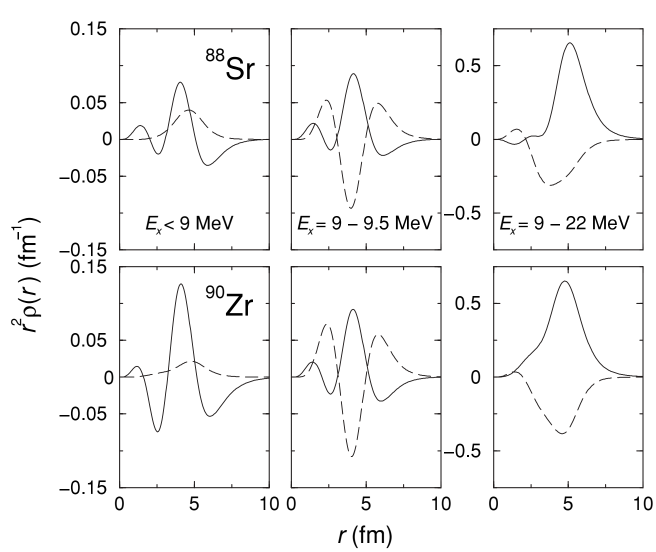

FIG. 14. Proton (solid lines) and neutron (dashed lines) transition densities in the $N = 50$ nuclei ^{88}Sr and ^{90}Zr.

features are characteristic for dipole skin modes, we identify these states as part of the PDR. The states in the region of E_x from 9 to 9.5 MeV carry a different signature and their contribution to the total proton and neutron transition densities in the energy region $E_x < 9.5$ MeV changes completely the behavior of the proton/neutron oscillations related to the PDR. At these higher energies the protons and neutrons start to move out of phase, being compatible with the low-energy part of the GDR. At E_x from 9 to 22 MeV a strong isovector oscillation corresponding to the excitation of the GDR is observed.

In the case of $N = 50$ isotones the neutron number is fixed and only the proton number changes. This affects the thickness of the neutron skin as well, as is seen in Fig. 11 and Table II. Correspondingly, the total PDR strength decreases with increasing proton number. According to the criteria just discussed we consider the states in the energy region $E_x <$ 9 MeV as a part of the PDR. In this energy interval, the QRPA calculations predict a total PDR strength of $\sum B(E1)\uparrow =$ $0.107\,e^2$ fm^2 in ^{90}Zr and $\sum B(E1)\uparrow = 0.170\,e^2$ fm^2 in ^{88}Sr, respectively. This accounts for 0.27% and 0.44% of the TRK in ^{90}Zr and ^{88}Sr, respectively, and compares with experimental values of 0.55(2)% and 0.74(2)% derived from resolved peaks in ^{90}Zr and ^{88}Sr, respectively, whereas the values deduced from the corrected full intensities including also the continuum part are remarkably greater and amount to 2.2(4)% and 2.4(6)% in ^{90}Zr and ^{88}Sr, respectively.

Finally, we note that the results are in agreement with the established connection between the calculated total PDR strength and the nuclear skin thickness, Eq. (9), found in our previous investigations in the $N = 82$ isotones [40] and the $^{100-132}$Sn isotope [32] nuclei.

In the multiphonon QPM calculations the structure of the excited states is described by wave functions as defined in Eq. (8). We now investigate multiphonon effects using a model space with up to three-phonon components, built from a basis of QRPA states with $J^\pi = 1^+, 1^-, 2^+, 3^-, 4^+, 5^-, 6^+, 7^-$, and 8^+. Because the one-phonon configurations up to $E_x =$ 22 MeV are considered the core polarization, contributions to the transitions of the low-lying 1^- states are taken into account explicitly. Hence, we do not need to introduce dynamical effective charges. Our model space includes one-, two-, and three-phonon configurations (in total 200) with energies up to $E_x = 12$ MeV.

The experimental absorption cross sections in ^{90}Zr in the range from 5 to 11 MeV are compared with the corresponding QPM results in Fig. 15. The strength in the region $E_x =$ 6–7 MeV is related to the PDR as identified from the structure of the involved 1^- states. The contribution of the GDR phonons becomes significant at energies $E_x > 7.5$ MeV where a coupling among PDR, GDR, and multiphonon states reflects the properties of the dipole excitations at higher energies. At low energy, the calculated values underestimate the experimental values derived from the full intensity and are close to the values deduced from resolved peaks only, whereas at high energy they are in better agreement with the experimental values including the full intensity. The calculated energy-weighted sum rule (EWSR) from 5 to 9 MeV of 1.3% of the TRK underestimates the experimental value of 2.2(4)%. However, by increasing the energy range to 11 MeV the

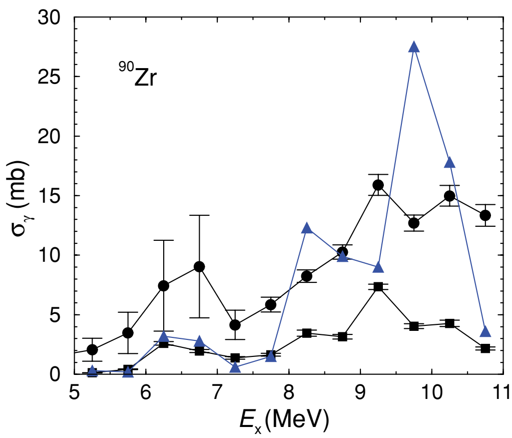

FIG. 15. (Color online) Experimental cross sections derived from resolved peaks (squares) and from the full intensity corrected for inelastic transitions and branching ratios (circles) and cross sections predicted by QPM calculations (blue triangles) for ^{90}Zr, averaged over energy bins of 0.5 MeV. Lines are drawn to guide the eye.

theoretical value of 3.3% is much closer to the experimental result of 4.0(3)%, indicating a slightly different distribution of the QPM strength with respect to excitation energy.

V. SUMMARY

The dipole-strength distribution in ^{90}Zr up to the neutron-separation energy has been studied in photon-scattering experiments at the ELBE accelerator by using various electron energies. Ground-state transitions have been identified by comparing the transitions observed at different electron energies. We identified about 190 levels with a total dipole strength of about 180 meV/MeV^3. Spin $J = 1$ could be deduced from the angular correlations of the ground-state transitions for about 140 levels including a dipole strength of about 155 meV/MeV^3.

The intensity distribution obtained from the measured spectra after a correction for detector response and a subtraction of atomic background in the target contains a continuum part in addition to the resolved peaks. It turns out that the dipole strength in the resolved peaks amounts to about 27% of the total dipole strength whereas the continuum contains about 73%.

An assignment of inelastic transitions to particular levels and thus the determination of branching ratios was in general not possible. To get information about the intensities of inelastic transitions to low-lying levels we have applied statistical methods. By means of simulations of γ-ray cascades, intensities of branching transitions could be estimated and subtracted from the experimental intensity distribution and the intensities of ground-state transitions could be corrected on average for their branching ratios.

A comparison of the photoabsorption cross section obtained in this way from the present (γ, γ') experiments with (γ, n) data shows a smooth connection of the data of the two different experiments and gives new information about the extension of the dipole-strength function toward energies around and below the threshold of the (γ, n) reaction. In comparison with a straightforward approximation of the GDR by a Lorentz curve one observes extra $E1$ strength in the energy range from 6 to 11 MeV, which is mainly concentrated in strong peaks.

QPM calculations in ^{88}Sr and ^{90}Zr predict low-energy dipole strength in the energy region from 6 to 10 MeV. The states at about 6 to 7.5 MeV have a special character. Their structure is dominated by neutron components and their transition strength is directly related to the size of a neutron skin. Their generic character is further confirmed by the shape and structure of the related transition densities, showing that these PDR modes are clearly distinguishable from the GDR. The dipole states, seen as a rather fragmented ensemble at $E_x > 7.5$ MeV, mix strongly with the low-energy tail of the GDR starting to appear in the same region. The complicated structure of these states and the high level densities impose considerable difficulties for a reliable description of the fragmentation pattern.

The present analysis shows that standard strength functions currently used for the calculation of reaction data do not describe the dipole-strength distribution below the (γ, n) threshold correctly and should be improved by taking into account the observed extra strength.

ACKNOWLEDGMENTS

We thank the staff of the ELBE accelerator for their cooperation during the experiments and we thank A. Hartmann and W. Schulze for their technical assistance. Valuable discussions with F. Dönau and S. Frauendorf are gratefully acknowledged. This work was supported by the Deutsche Forschungsgemeinschaft under Contract Nos. Do466/1-2 and Le439/4-3.

[1] P. Axel, K. K. Min, and D. C. Sutton, Phys. Rev. C **2**, 689 (1970).
[2] S. Datta and J. S. Allen, Phys. Rev. C **8**, 1421 (1973).
[3] R. M. Laszewski, R. Alarcon, and S. D. Hoblit, Phys. Rev. Lett. **59**, 431 (1987).
[4] R. Alarcon, R. M. Laszewski, A. M. Nathan, and S. D. Hoblit, Phys. Rev. C **36**, 954 (1987).
[5] U. Kneissl, N. Pietralla, and A. Zilges, J. Phys. G: Nucl. Part. Phys. **32**, R217 (2006).
[6] R. Schwengner, R. Beyer, F. Dönau, E. Grosse, A. Hartmann, A. R. Junghans, S. Mallion, G. Rusev, K. D. Schilling, W. Schulze, and A. Wagner, Nucl. Instrum. Methods A **555**, 211 (2005).
[7] R. Schwengner, G. Rusev, N. Benouaret, R. Beyer, M. Erhard, E. Grosse, A. R. Junghans, J. Klug, K. Kosev, L. Kostov, C. Nair, N. Nankov, K. D. Schilling, and A. Wagner, Phys. Rev. C **76**, 034321 (2007).
[8] G. Rusev, R. Schwengner, F. Dönau, M. Erhard, E. Grosse, A. R. Junghans, K. Kosev, K. D. Schilling, A. Wagner, F. Bečvář, and M. Krtička, Phys. Rev. C **77**, 064321 (2008).
[9] F. R. Metzger, Nucl. Phys. **A182**, 213 (1972).
[10] F. R. Metzger, Phys. Rev. C **9**, 1525 (1974).

[11] L. E. Cannell, thesis, University of Illinois, 1976 (unpublished).
[12] E. Browne, Nucl. Data Sheets **82**, 379 (1997).
[13] U. E. P. Berg, J. Phys. (Paris), Colloq. **C4**, 359 (1984).
[14] F. Ajzenberg-Selove and J. H. Kelley, Nucl. Phys. **A506**, 1 (1990).
[15] CERN Program Library Long Writeup W5013, Geneva, 1993 (unpublished).
[16] E. Haug, Radiat. Phys. Chem. **77**, 207 (2008).
[17] G. Roche, C. Ducos, and J. Proriol, Phys. Rev. A **5**, 2403 (1972).
[18] F. Salvat, J. D. Martinez, R. Mayol, and J. Parellada, Phys. Rev. A **36**, 467 (1987).
[19] C. E. Porter and R. G. Thomas, Phys. Rev. **104**, 483 (1956).
[20] G. Rusev, dissertation, Technische Universität Dresden, 2007, Report FZD-478 (ISSN 1437-322X), http://fzd.de/publications/010008/10008.pdf.
[21] F. Bečvář, Nucl. Instrum. Methods A **417**, 434 (1998).
[22] T. von Egidy and D. Bucurescu, Phys. Rev. C **72**, 044311 (2005).
[23] T. A. Brody, J. Flores, J. B. French, P. A. Mello, A. Pandey, and S. S. M. Wong, Rev. Mod. Phys. **53**, 385 (1981).
[24] Y. Kalmykov, T. Adachi, G. P. A. Berg, H. Fujita, K. Fujita, Y. Fujita, K. Hatanaka, J. Kamiya, K. Nakanishi, P. von Neumann-Cosel, V. Yu. Ponomarev, A. Richter, N. Sakamoto, Y. Sakemi, A. Shevchenko, Y. Shimbara, Y. Shimizu, F. D. Smit, T. Wakasa, J. Wambach, and M. Yosoi, Phys. Rev. Lett. **96**, 012502 (2006).
[25] Y. Kalmykov, C. Özen, K. Langanke, G. Martínez-Pinedo, P. von Neumann-Cosel, and A. Richter, Phys. Rev. Lett. **99**, 202502 (2007).
[26] P. Axel, Phys. Rev. **126**, 671 (1962).
[27] B. L. Berman, J. T. Caldwell, R. R. Harvey, M. A. Kelly, R. L. Bramblett, and S. C. Fultz, Phys. Rev. **162**, 1098 (1967).
[28] P. Ring and P. Schuck, *The Nuclear Many Body Problem* (Springer-Verlag, Berlin, Heidelberg, 1980).
[29] T. Belgya, O. Bersillon, R. Capote, T. Fukahori, G. Zhigang, S. Goriely, M. Herman, A. V. Ignatyuk, S. Kailas, A. Koning, P. Oblozinsky, V. Plujko, and P. Young, *Handbook for Calculations of Nuclear Reaction Data, RIPL-2*, IAEA-TECDOC-1506 (IAEA, Vienna, 2006); http://www-nds.iaea.org/RIPL-2/.
[30] A. J. Koning, S. Hilaire, and M. C. Duijvestijn, AIP Conf. Proc. **769**, 1154 (2005).
[31] N. Tsoneva, H. Lenske, and Ch. Stoyanov, Phys. Lett. **B586**, 213 (2004).
[32] N. Tsoneva and H. Lenske, Phys. Rev. C **77**, 024321 (2008).
[33] V. G. Soloviev, *Theory of Complex Nuclei* (Pergamon, Oxford, 1976).
[34] G. Audi and A. H. Wapstra, Nucl. Phys. **A595**, 409 (1995).
[35] F. Hofmann and H. Lenske, Phys. Rev. C **57**, 2281 (1998).
[36] A. Vdovin and V. G. Soloviev, Sov. J. Part. Nucl. **14**, 99 (1983).
[37] M. Grinberg and Ch. Stoyanov, Nucl. Phys. **A573**, 231 (1994).
[38] N. Ryezayeva, T. Hartmann, Y. Kalmykov, H. Lenske, P. von Neumann-Cosel, V. Yu. Ponomarev, A. Richter, A. Shevchenko, S. Volz, and J. Wambach, Phys. Rev. Lett. **89**, 272502 (2002).
[39] P. Adrich, A. Klimkiewicz, M. Fallot, K. Boretzky, T. Aumann, D. Cortina-Gil, U. Datta Pramanik, Th. W. Elze, H. Emling, H. Geissel, M. Hellström, K. L. Jones, J. V. Kratz, R. Kulessa, Y. Leifels, C. Nociforo, R. Palit, H. Simon, G. Surowka, K. Sümmerer, and W. Walus, Phys. Rev. Lett. **95**, 132501 (2005).
[40] S. Volz, N. Tsoneva, M. Babilon, M. Elvers, J. Hasper, R.-D. Herzberg, H. Lenske, K. Lindenberg, D. Savran, and A. Zilges, Nucl. Phys. **A779**, 1 (2006).
[41] A. Bohr and B. Mottelson, *Nuclear Structure II* (W. A. Benjamin, Inc., Reading, Massachusetts, 1975).